Published online June 23, 2004

3364–3375 *Nucleic Acids Research, 2004, Vol. 32, No. 11*
DOI: 10.1093/nar/gkh664

Rna14–Rna15 assembly mediates the RNA-binding capability of *Saccharomyces cerevisiae* cleavage factor IA

Christian G. Noble, Philip A. Walker, Lesley J. Calder[1] and Ian A. Taylor*

Division of Protein Structure and [1]Division of Virology, National Institute for Medical Research, The Ridgeway, Mill Hill, London NW7 1AA, UK

Received April 20, 2004; Revised May 13, 2004; Accepted June 4, 2004

ABSTRACT

The Rna14–Rna15 complex is a core component of the cleavage factor IA RNA-processing complex from *Saccharomyces cerevisiae*. To understand the assembly and RNA-binding properties, we have isolated and characterized the Rna14–Rna15 complex using a combination of biochemical and biophysical methods. Analysis of the purified complex, using transmission electron microscopy, reveals that the two proteins assemble into a kinked rod-shaped structure and that these rods are able to further self-associate. Analytical ultracentrifugation reveals that Rna14 mediates this association and facilitates assembly of an A_2B_2 tetramer (M_r 230 000), where relatively compact Rna14–Rna15 heterodimers are in rapid equilibrium with tetramers that have a more extended shape. The Rna14–Rna15 complex, unlike the individual components, binds to an RNA oligonucleotide derived from the 3′-untranslated region of the *S.cerevisiae GAL7* gene. Based on these structural and thermodynamic data, we propose that CFIA assembly regulates RNA-binding activity.

INTRODUCTION

The alternative processing of the transcript of a single gene results in a great degree of diversity both at the level of the transcriptome and the proteome. The most obvious and well-characterized mechanism by which this occurs is splice variation; up to 60% of genes in the mouse genome may undergo alternative splicing (1). It is also becoming increasingly apparent that alternative 3′ end processing of nascent RNAs is widespread. Up to 40% of human genes appear to contain alternative polyadenylation signals (2,3), and this percentage could be even higher if alternative sites that occur at long range are taken into account (4). The presence of multiple polyadenylation sites allows the production of transcripts with alternative 3′-untranslated regions (3′-UTRs) and in some cases this results in the translation of a variant protein sequence (5). More generally, the 3′-UTR contains many of the regulatory elements that control properties, such as transcript stability, nuclear export, translational efficiency and subcellular localization of the mature mRNA (6). Alternative processing in the 3′-UTR can be used to control both the level and localization of gene expression and so is responsible for regulating many of the events that occur during development, cellular differentiation and tissue-specific gene expression. Given the importance of alternative 3′ processing for the regulation of gene expression, it is vital to understand the mechanism of both cleavage site selection and the efficiency of cleavage/polyadenylation.

In *Saccharomyces cerevisiae*, cleavage factor I (CFI) is an essential component of the polyadenylation machinery. This multisubunit complex is required for cleavage site selection and recruitment of other proteins required to initiate transcript cleavage and polyadenylation (7). The CFI complex consists of five proteins but can be resolved by gel filtration into two subcomplexes, CFIA and CFIB (8). CFIA contains four subunits Rna14, Rna15, Pcf11 and Clp1. CFIB is a single protein, Hrp1. An increasing amount of evidence suggests that the cleavage and polyadenylation reactions are conserved from yeast to mammals; all of the CFIA components have mammalian homologues (7,9,10). Rna14 and Rna15 are homologous to two of the components of the mammalian cleavage stimulatory factor, CstF-77 and CstF-64, respectively. Clp1 and Pcf11 are homologous to hClp1 and hPcf11, components of human CFII (11). Therefore, the yeast system is likely to be a good model for the human complex.

Some of the properties of CFIA components have been characterized. Pcf11 is a 72 kDa protein and contains a CTD-interaction domain (CID) at its N-terminus responsible for binding in a phospho-dependant manner to the C-terminal domain of Rpo21, the largest subunit of RNA polymerase II (12–14). Data from yeast two-hybrid analysis has identified other sequences within Pcf11 that are responsible for interaction with Rna14 and Rna15 (15,16). Relatively little is known about Clp1, the 50 kDa component of CFIA, but it contains Walker A and B motifs, suggesting that it may have nucleotide-binding properties (11). The other two components of CFIA, Rna14 and Rna15, interact directly with each other. This association has been demonstrated both *in vivo* and *in vitro* (17,18) and more recently by their co-purification in large-scale epitope tagging experiments (19,20). Rna14 is an 80 kDa protein and contains 10 HAT (half a TPR) repeats. Intriguingly, all proteins containing HAT repeats identified so far are components

*To whom correspondence should be addressed. Tel: +44 020 88162552; Fax: +44 020 88162580; Email: itaylor@nimr.mrc.ac.uk

of RNA-processing complexes. It is likely that they are involved in the protein–protein interactions required for complex assembly (21). Rna15 is a 33 kDa protein containing a single RNA recognition motif (RRM) at the N-terminus and a C-terminal region essential for efficient transcriptional termination and polyadenylation (22). The RNA-binding activity of Rna15 has been demonstrated using UV cross-linking techniques (23,24) and by affinity chromatography using immobilized polyuridylic acid (25). However, evidence for a specific Rna15–RNA interaction could only be obtained in the presence of both Rna14 and Hrp1 (23). Recently, Rna15 has been implicated in other modes of transcriptional regulation, since it has been shown to be associated with transcriptional activators (26) and co-activators (27).

Given the role that polyadenylation site selection and 3′ end processing have in generating and regulating transcriptome diversity, a full understanding of the makeup of the protein complexes and their interactions is important. Here, we report a series of *in vitro* physical studies investigating the Rna14–Rna15 complex, a core component of CFIA. We show that Rna15 associates tightly with Rna14 to form a heterodimeric complex and that this association is required for RNA binding to occur. Using hydrodynamic methods, we show that these Rna14–Rna15 heterodimers can self-associate further to form tetramers, through an interface largely within Rna14. Electron microscopy studies reveal the overall shape and size of the Rna14–Rna15 complex and provide further insight into tetramerization. Finally, we present a model for how complex assembly mediates RNA-binding.

MATERIALS AND METHODS

Protein expression and purification

The DNA sequence coding for Rna15 was isolated by PCR amplification from the *S.cerevisiae* genome. DNA fragments corresponding to the full-length protein, residues 1–94 (Rna15NtD) and residues 127–296 (Rna15CtD), were inserted into the NdeI and XhoI sites of a pET22b expression vector (Novagen) in order to produce C-terminal hexa-histidine fusions. The nucleotide sequence of each expression clone was verified by automated DNA sequencing. Proteins were expressed in the *Escherichia coli* strain BL21 (DE3) and were purified from clarified crude cell extracts using combinations of ion-exchange, immobilized metal-ion-affinity and gel-filtration chromatography. For co-expression of Rna14 and Rna15, the two genes were inserted into pET-Duet-1 (Novagen). In this construct, Rna14 was fused to an N-terminal hexa-histidine sequence and inserted 5′ to the native Rna15 sequence. The protein complex was then purified in a similar manner to the Rna15 constructs. Rna14 was also overexpressed and purified from a baculovirus system. Here, the Rna14 gene was inserted in frame into the NcoI and XhoI sites of pFASTBac-Htb to produce a N-terminal His-tag fusion. A correct clone was verified by DNA sequencing and a recombinant bacmid produced by transposition following the manufacturer's instructions (Invitrogen). The resulting virus at a titre of $\sim 10^8$ pfu/ml was used to infect 2 litres of Sf9 cells (density of 5×10^5 cells/ml) at a MOI of 3:1. The culture was grown for 72 h post-infection and the cells were harvested by centrifugation. Rna14 was then purified from the clarified insect cell extract in a manner similar to the bacterially expressed proteins. The purity and monodispersity of preparations were monitored by ESI–MS, SDS–PAGE, photon correlation spectroscopy and analytical size-exclusion chromatography. Protein concentrations were determined from the absorbance at 280 nm using molar extinction coefficients derived by summing the contributions from tyrosine and tryptophan residues. The values derived in this manner are Rna15, 19 200; Rna15NtD, 6500; Rna15CtD, 11 400; Rna14-bac, 125 600 and Rna14–Rna15 heterodimer 139 600.

Electron microscopy

Rna14–Rna15 complex was prepared for electron microscopy by dialysis into 20 mM Tris–HCl, pH 7.5, 50 mM NaCl, 0.5 mM Tris[2-carboxyethylphosphine] hydrochloride (TCEP). The sample at a concentration of 0.2 mg/ml was adsorbed to carbon-coated grids and negatively stained with 1% sodium silicotungstate, pH 7.0. The grids were viewed with a Jeol 1200 electron microscope operated at 100 kV under minimum dose accurate defocus conditions. Micrographs were taken at a nominal 30 000× magnification regularly calibrated using catalase crystals. Molecular measurements were made using photographic prints at a 200 000× final magnification.

Determination of Rna14–Rna15 subunit stoichiometry

The concentration of a sample of purified Rna14–Rna15 complex was determined by UV spectroscopy using extinction coefficients derived by assuming differing Rna14:Rna15 stoichiometries of 1:1, 2:1, 1:3 and 1:4. Using these apparent concentrations, samples of the complex were loaded onto an SDS–polyacrylamide gel in order to give loadings of 1.5, 1.0 and 0.5 μg of Rna15. On the same gel, 1.5, 1.0 and 0.5 μg of His-tagged Rna15 was also loaded. The gels were stained with Coomassie blue and, after appropriate background subtraction, the integrated intensity of each band was determined. The stoichiometry of the purified Rna14–Rna15 complex was also analysed by automated Edman degradation (Babraham Bioscience Technologies Ltd). Three cycles of the reaction were carried out and the pmol quantity of each residue released determined by integration of the HPLC peak.

Sedimentation velocity

Sedimentation velocity experiments were performed in a Beckman Optima XLA analytical ultracentrifuge using conventional double sector quartz cells in an An-60 Ti rotor. The rotor speed was 35 000 r.p.m. and the temperature was maintained at 293 K. Protein partial specific volumes and the solvent density were calculated from tabulated values (28). Prior to centrifugation, protein samples were dialysed exhaustively against the buffer blank 20 mM Tris–HCl, pH 7.5, 150 mM NaCl, 0.5 mM TCEP. Experiments were carried out at protein concentrations varying from 0.3 to 0.6 mg/ml and radial scans, $\lambda = 280$ nm, were collected every 600 s. The data recorded from moving boundaries were analysed in terms of a single-species model, rapid monomer–dimer self-association or to the continuous size distribution functions, C(S) and C(M) using the program SEDFIT (29,30).

Sedimentation equilibrium

Sedimentation equilibrium experiments were performed in a Beckman Optima XLA analytical ultracentrifuge using six-channel centrepieces in an An-60 Ti rotor. Prior to centrifugation, samples were dialysed exhaustively against the buffer blank, 20 mM Tris–HCl, pH 7.5, 150 mM NaCl, 0.5 mM TCEP. After centrifugation for 18 h, cells were scanned radially at 2 h intervals (λ = 280 and 250 nm) until no further change in the absorbance profile was observed. The rotor speed was then increased and the procedure repeated. Usually data were collected at three speeds along with scans at 42 000 r.p.m. to determine any residual absorbance to set initial offset values. The program ORIGIN was used to determine weight-averaged molecular weights by non-linear fitting of the final equilibrium profiles (*A* versus *r*) to a single-species ideal-solution model. Where no concentration dependence was observed, global fitting incorporating data from different speeds and sample concentrations was applied to extract the final molecular weight. Where concentration dependence was evident, the data scans at multiple speeds and sample concentrations were fitted globally to a monomer–dimer equilibrium model.

Ribo-oligonucleotides

Ribo-oligonucleotides, derived from the 3′-UTR of the *S.cerevisiae GAL7* gene, were purchased gel-purified from Oswel DNA services (University of Southampton, UK): CAC-C**UAUAUAUUUAAUAAU**UAA (*GAL7*-UTR); CACCGAGAC-GCGCGACAGACAA (C-rich). The sequence in boldface is derived from the 3′-UTR of *S.cerevisiae GAL7*. The molar extinction coefficient at 260 nm was determined for the ribo-oligonucleotide by summing the contribution from the individual nucleotides, taking into account the hyperchromicity observed following digestion by snake venom phosphodiesterase I (31). Using this method, values of ε_{260} = 254 400 for *GAL7*-UTR and 189 048 for C-rich were determined.

Surface plasmon resonance

The *GAL7*-UTR ribo-oligonucleotide was synthesized with a biotin group at the 5′ end (Oswel) and was attached to a streptavidin-coated sensor chip (Biacore). A buffer of 10 mM Tris–HCl, pH 7.8, 150 mM NaCl, 3 mM EDTA and 0.005% Tween-20 (v/v) was flowed across the chip until the trace levelled off. The 22mer was then attached to flow cell 2 by injecting 100 µl of 100 nM 22mer in 0.3 M NaCl across the chip at 5 µl/min. Flow cell 2 and a blank (flow cell 1) were blocked with 100 µl of 1 mg/ml biotin at 5 µl/min. A buffer of 40 mM Tris–HCl, pH 7.8, 40 mM NaCl, 5 mM $MgCl_2$, 4 mM DTT, 5% (v/v) glycerol and 0.002% (v/v) Tween-20 was flowed across flow cells 1 then 2. Typically, 100 µl of 5–80 nM protein sample was injected into the same buffer across the chip at 30 µl/min. Experiments were performed on a Biacore 2000 instrument. The data were fitted to a 1:1 binding model using BIAevaluation 3.0.

Gel retardation assays

Typically ~1 nmole of a ribo-oligonucleotide was end labelled using [γ-^{32}P]ATP and T4 polynucleotide kinase with standard protocols. The labelled RNA was purified from unincorporated ATP using a Probe quant spin column (Amersham Biosciences) and then ethanol precipitated. Labelled RNA was resuspended in 10 mM Tris–HCl, 1 mM EDTA, pH 8.0. The concentration was then determined accurately from the absorbance at 260 nm. RNA-binding reactions were carried out in a binding buffer containing 10% glycerol, 5 mM $MgCl_2$, 4 mM DTT, 40 mM Tris–HCl, pH 8.0. Increasing amounts of protein were incubated with a fixed concentration of labelled RNA (~1 µM) and the free and bound components of the equilibria resolved by electrophoresis at 14 mA constant current for 45 min on a 4–10% acrylamide gradient, native TAE gel (40 mM Tris-acetate, 1 mM EDTA, pH 8.5). The labelled components were visualized either by autoradiography or by phosphorimaging.

RNA–protein UV cross-linking

In a typical assay, 10 µl samples of 0.25 µM ^{32}P-labelled RNA were combined with 0.25–2 µM Rna15 or Rna14–Rna15 complex and incubated on ice in 72 well minitrays (Nunc). The samples were irradiated with a handheld 25 W 254 nm UV light at a distance of 5 cm for 5 min and the products resolved by SDS–PAGE. The gels were stained with Coomassie blue to visualize protein components and then dried and the radiolabelled components visualized by either autoradiography or by phosphorimaging.

RESULTS

Overall structure of the complex

Co-expressed Rna14 and Rna15 co-purify through three steps of chromatographic separation. These steps include nickel-affinity chromatography exploiting the His-tag present on Rna14 and a high-resolution ion-exchange chromatography step using Source Q. During these procedures, and the final purification by size-exclusion chromatography, separation of the two proteins was not observed. The apparent absence of dissociation, even under the non-equilibrium conditions of the purification procedures, indicates that Rna14 and Rna15 are assembled into a tight complex. A similar observation is made when CFIA is purified from budding yeast (8). The size of the Rna14–Rna15 complex has allowed its examination by transmission electron microscopy, using negative staining; a typical field is shown in Figure 1A. Enlargements of some of the particles found in this field are shown in Figure 1B and sketches of the molecules are shown in Figure 1C. The complexes appear as rod-shaped particles containing a distinct bend or kink of ~110°. The kink is somewhat off centre in the particle, giving rise to a short arm, ~80 Å in length and a long arm ~100 Å in length (Figure 1D). Interestingly, single-kinked rods only account for ~60% of molecules in a typical field. The remainder appears to be a dimeric form of these kinked rods that are associated near to the tip of their short arm. It is apparent that whilst the basic bent shape of individual heterodimers appears to be constant, the orientation between the pairs of associated heterodimers seems variable, indicating flexibility at the interface between individual particles.

Stoichiometry of the Rna14–Rna15 complex

Although Rna14 and Rna15 co-purify as a complex, the stoichiometry of Rna14 to Rna15 within the complex was

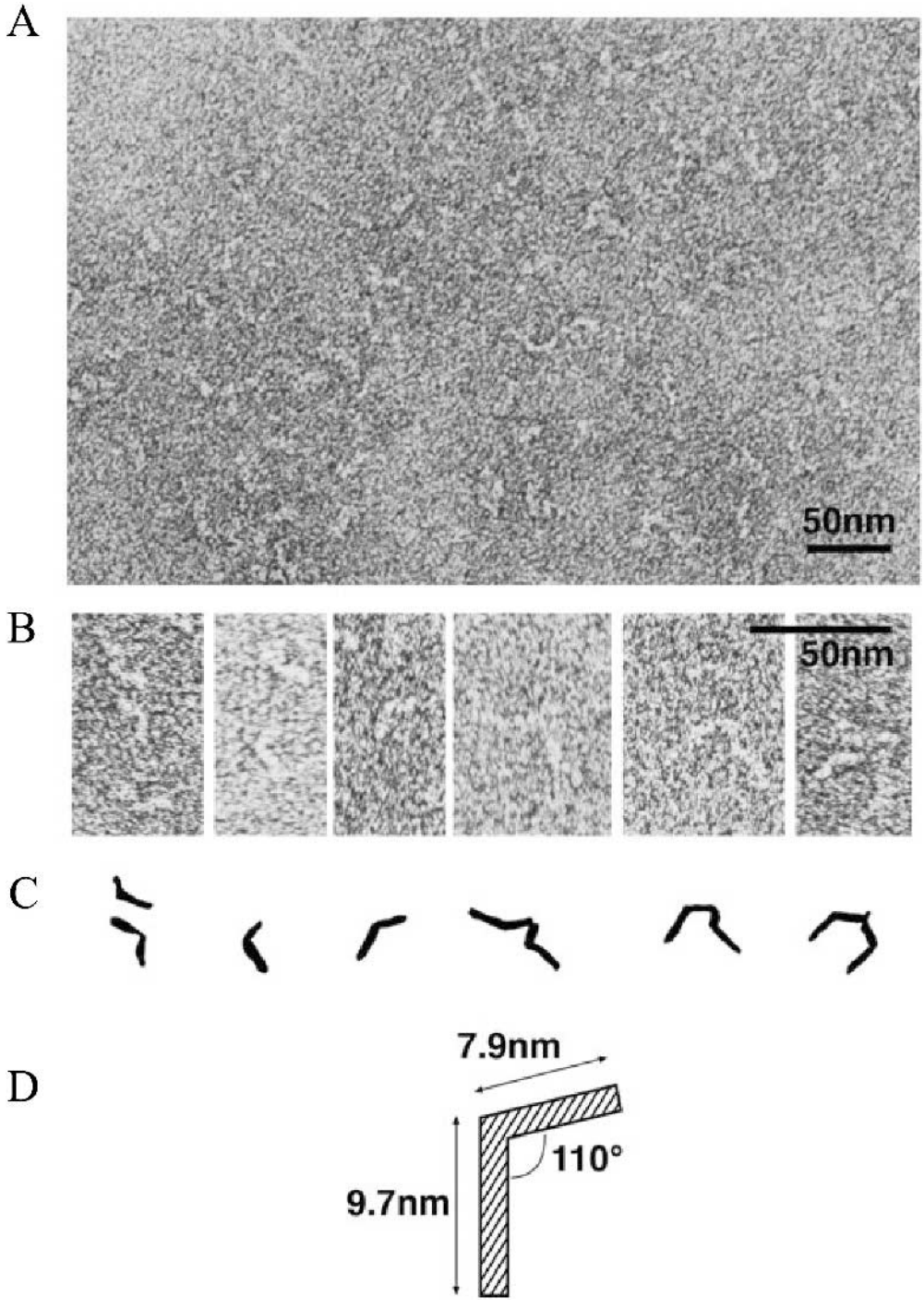

Figure 1. Transmission electron micrograph of negatively stained Rna14–Rna15 particles. (**A**) A typical field of Rna14–Rna15 particles. (**B**) Individual Rna14–Rna15 particles, illustrating the different classes and orientation of particles observed. (**C**) Sketches of the various particles shown in the panels above. (**D**) Molecular dimensions of a single Rna14–Rna15 particle.

unknown. Initial analysis using dynamic light scattering gave an estimated molecular weight of ~260 kDa and provided no insight into the stoichiometry of the complex. Therefore, two further complementary approaches were used. First, three cycles of Edman degradation sequencing were carried out on a sample of Rna14–Rna15 complex (Figure 2A). At each cycle of the reaction, approximately equal amounts of amino acid derived from each chain are released, indicating a 1:1 stoichiometry of these polypeptides within the complex. Second, the complex was analysed using scanning densitometry of Coomassie-stained proteins resolved by SDS–PAGE (Figure 2B and C). In this experiment, the band intensities for a sample of the complex where the concentration was determined assuming a stoichiometry of 1:1, best matches the control loadings of Rna15. Taken together, these data suggest that in the absence of the other CFI components,

A

Chain	Cycle 1 (pmole)	Cycle 2 (pmole)	Cycle 3 (pmole)	[1]pmole(0)	E
Rna14	20.32 (G)	15.15 (S)	14.64 (S)	23.60	0.84
Rna15	20.28 (M)	17.69 (N)	22.10 (R)	20.93	0.96

1) N-terminal sequencing data was fitted to the expression pmole(n) = pmole(0)E^n. Here pmole(n) is amount of amino acid released at cycle n, E is the efficiency of the sequencing reaction and pmole(0) is the amount of each chain in the starting material.

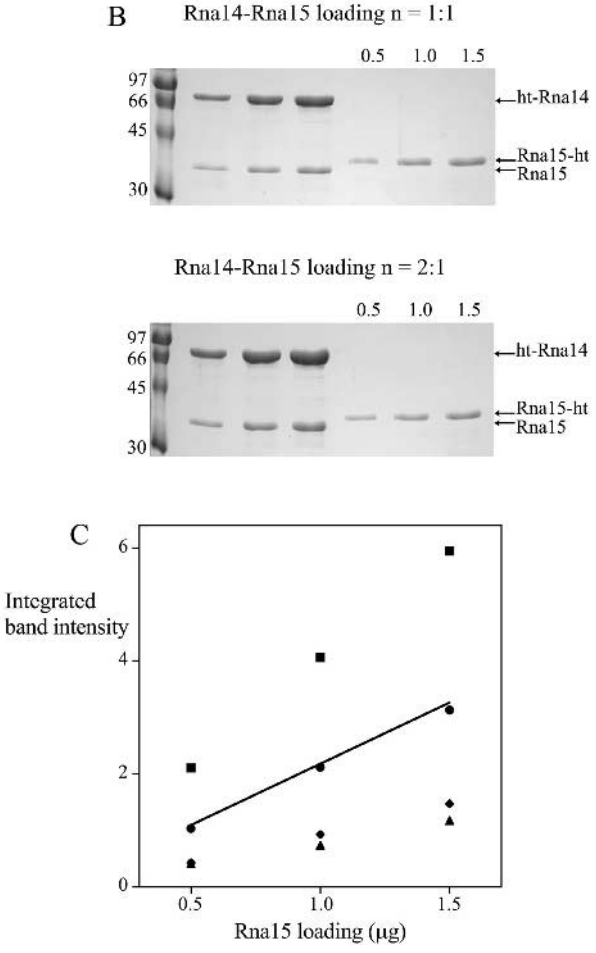

Figure 2. The determination of the Rna14–Rna15 subunit stoichiometry. (**A**) N-terminal analysis of recombinant Rna14–Rna15 complex. Three cycles of Edman degradation were carried out on a sample of purified Rna14–Rna15. The table shows the yield of each residue at each cycle and the pmol quantity of each chain. Accounting for the reaction efficiency (E) a value for the quantity of each chain in the starting material, pmol(0) was also determined. (**B**) SDS gels used in the densitometric analysis. Top, loadings of complex with an assumed stochiometry of 1:1. Bottom, loadings of complex with an assumed stoichiometry of 2:1. (**C**) Densitometric analysis of Rna14–Rna15 stoichiometry. Integrated band intensity is plotted against calculated Rna15 loading for complexes with assumed Rna14:Rna15 stoichiometries of 2:1, square; 1:1, circle; 1:3, diamond; and 1:4, triangle. The straight line is the best fit to actual RNA15-ht loadings of 0.5, 1.0 and 1.5 μg. Rna15-ht and ht-Rna14 indicate C- and N-terminally His-tagged Rna15 and Rna14, respectively.

Rna14 interacts stoichiometrically with Rna15 to form a tight complex.

Associative behaviour of component proteins

Sedimentation equilibrium experiments were carried out on Rna14, Rna15, Rna15NtD, Rna15CtD as well as the Rna14–Rna15 complex. Typical fits to the data are shown in Figure 3 and the results are summarized in Table 1. Rna15 and its individual N- and C-terminal domains display the sedimentation behaviour of non-interacting particles. Over the concentration range of the experiment, there is little or no trend in the apparent molecular weight. Consequently, good fits were obtained in all of these cases to ideally behaving single species with weight-averaged molecular weights (M_w) in close agreement with the formula molecular mass (M_r). The sedimentation behaviour observed for Rna14 and the Rna14–Rna15 complex is somewhat different. First, a fit to a single-species model for the Rna14–Rna15 complex yields a molecular weight of 140–205 kDa. These values are very difficult to reconcile with the observed 1:1 subunit stoichiometry (M_r Rna14 + Rna15 = 114 kDa). Taking into account the tight association between Rna14 and Rna15 and the stoichiometric ratio, this suggests that the data need to be analysed in terms of a self-association model in which one Rna14–Rna15 heterodimer interacts with another to form a tetramer containing two copies of each protein. The data fit well to this type of model with an association constant of $\sim 6 \times 10^5$ M^{-1}. The Rna14 protein alone shows similar behaviour. In this case, fitting to a single-species model results in weight-averaged molecular weights of ~145 kDa (M_r Rna14 = 83 kDa). Analysing these data in terms of Rna14 homodimerization yields an association constant of $\sim 2 \times 10^6$ M^{-1} and suggests that Rna14 is responsible for the association of Rna14–Rna15 heterodimers.

Sedimentation velocity experiments were employed to characterize the dimer–tetramer equilibrium between heterodimers and to examine the molecular shape. The velocity data were analysed using finite element solutions to the Lamm equation for a single-species model, a rapidly associating dimer–tetramer model and the continuous size distribution functions C(S) and C(M) (Table 2). C(S) and C(M) respectively provide a distribution of sedimentation coefficients or weight-averaged molecular weights that best fit the data, rather than solving the Lamm equation to obtain a single value for each. This type of analysis is particularly useful where the sample may contain a mixture of components. The sedimentation velocity data fit well to a single-component model with $S_{20,w}$ = 8.1 and $D_{20,w}$ = 3.7 × 10^{-7} cm^2/s and gives rise to an apparent molecular weight of 196 800 kDa and a corresponding frictional ratio of 1.51. Since the sedimentation equilibrium and transmission electron microscopy studies show that the sample is a mixture of species, the data were also fitted using the continuous size distribution functions C(S) and C(M) (Figure 4). A very tight distribution centred on S_{app} of 7.8 corresponding to $S_{20,w}$ of 8.1 is obtained from the C(S) analysis. Similarly, the C(M) analysis also reveals only a single tight distribution for the weight-averaged molecular weight with a peak at 194 700 kDa, intermediate between the heterodimer and the heterotetramer. Finally, the data were analysed using a rapidly associating dimer–tetramer model. The data also fit well to this type of model and allow the extraction of shape parameters for the dimer and tetramer components of the equilibrium together with the association constant. Using this type of analysis, it is immediately apparent that the dimer and tetramer have similar values of $S_{20,w}$ giving rise to very dissimilar frictional ratios of 1.15 and 1.61. This large difference in the

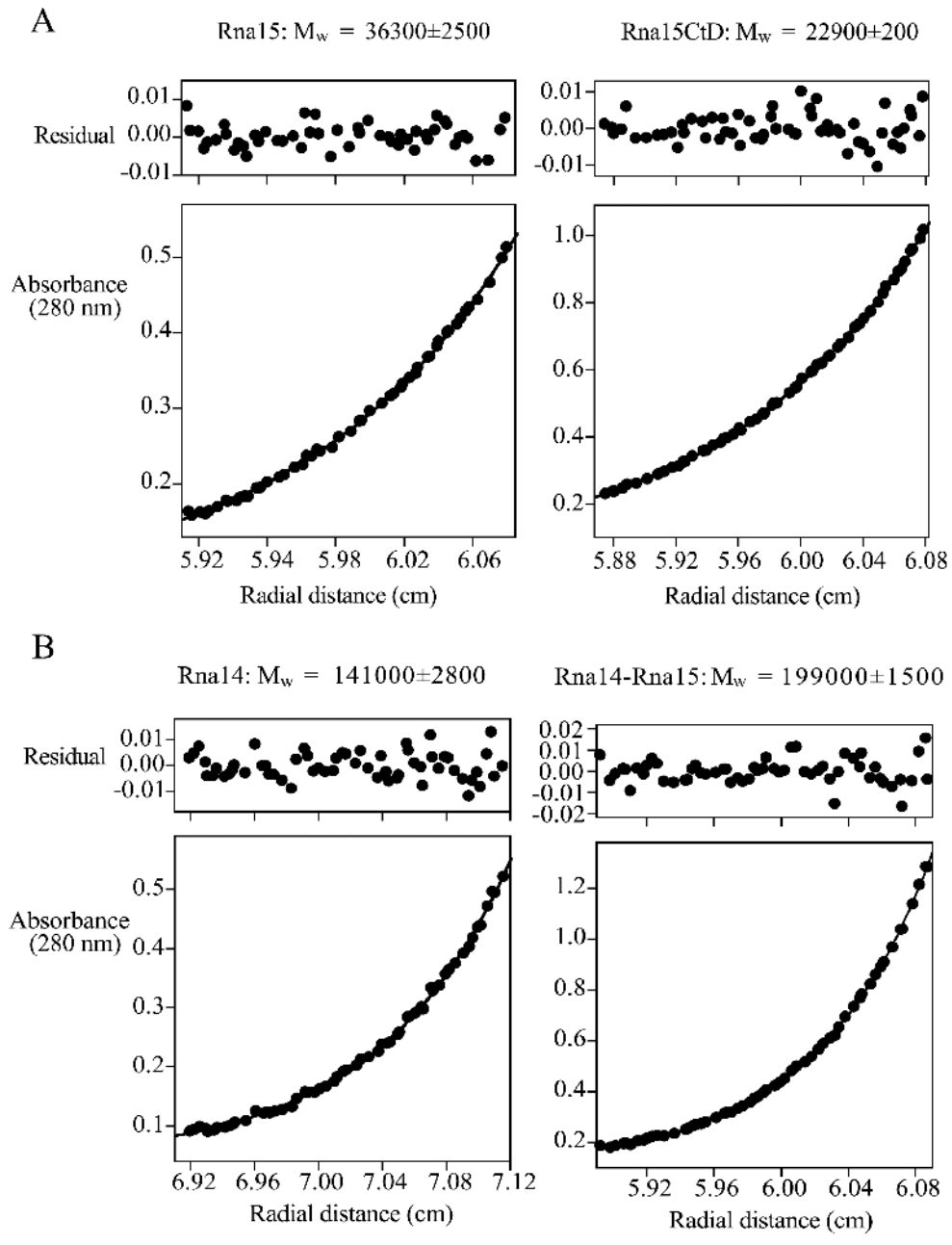

Figure 3. Analysis of Rna14 and Rna15 by sedimentation equilibrium. (**A**) Bottom panels are typical concentration distributions at sedimentation equilibrium for 17 μM Rna15 at 17 000 r.p.m. and 44 μM Rna15CtD at 22 000 r.p.m. (**B**) Bottom panels are the concentration distribution at sedimentation equilibrium for 2.1 μM Rna14 and 5.7 μM Rna14–Rna15 at 10 000 r.p.m. The curves are the best fit to these data and the top panels are the residuals to this fit. The weight-averaged molecular weight, M_w, derived from global fitting, is shown above each.

frictional ratios suggests that the tetramer is more extended or asymmetric than the dimer, agreeing with the electron microscopy images. The good fit to the single-component model, and C(S) and C(M) functions presumably result from averaging due to rapid reversible association of two components that have similar sedimentation coefficients.

RNA-binding characteristics

The RNA-binding properties of Rna14 and Rna15 were investigated using a combination of surface plasmon resonance (SPR), UV cross-linking and gel retardation experiments. For SPR, a 22mer ribo-oligonucleotide containing both the UA-rich and A-rich elements from the 3′-UTR of *S.cerevisiae GAL7* was attached to the surface of a biosensor chip by means of a 5′ biotin coupled through immobilized streptavidin. Rna15, Rna15NtD (the RRM domain) and Rna14 were then analysed for their ability to bind to the ribo-oligonucleotide (Figure 5A). At the nanomolar concentrations used in this experiment, Rna15 and Rna14 show no obvious signs of interaction with the immobilized RNA. Moreover, no detectable binding is observed using the isolated RRM domain,

Table 1. Summary of sedimentation equilibrium data

Protein	M_r	ν (ml/g)	ρ (g/ml)	M_w	Fit variance	C range (μM)	K_a (M^{-1})[a]
Rna15[b]	33 856	0.725	1.005	36 300 ± 2500	1.4×10^{-5}	8–17	—
Rna15NtD[c]	11 476	0.721	1.005	11400 ± 400	2×10^{-5}	25–140	—
Rna15CtD[d]	19 974	0.737	1.005	22 900 ± 200	2×10^{-5}	18–100	—
Rna14[e]	83 025	0.730	1.007[f]	145 000 ± 3000	2.6×10^{-5}	0.66–2.52	$2 \times 10^6 \pm 20\%$
Rna14–Rna15 (1:1)[g]	114 058	0.729	1.005	140 000–205 000	$3–5 \times 10^{-5}$	1–11	$6 \times 10^5 \pm 20\%$

[a]The equilibrium constants determined directly from absorbance data are expressed in the form of absorbance units termed $K_{a,abs}$. Actual equilibrium constants, expressed on a molar basis, K_a were converted from $K_{a,abs}$ by the application of the expression $K_a = \varepsilon_\lambda l K_{a,abs}/2$ taking into account the extinction coefficient ε_λ of the sample and the optical pathlength of the cell (12 mm).
[b]Rna15 molecular weight data were derived from global fitting of sedimentation equilibrium absorbance data (λ = 280 nm). The data were collected at three sample concentrations using rotor speeds of 14 000, 17 000 and 19 000. The final global fit incorporates data from nine independent measurements.
[c]Rna15NtD molecular weight data were derived by global fitting of sedimentation equilibrium absorbance data (λ = 280 and 250 nm). The data were measured at nine sample concentrations using rotor speeds of 22 000, 26 000 and 30 000. The final global fit incorporates data from 15 independent measurements.
[d]Rna15CtD molecular weight data were derived by global fitting of sedimentation equilibrium absorbance data (λ = 280 and 250 nm). The data were measured at nine sample concentrations using rotor speeds of 18 000, 20 000 and 22 000. The final global fit incorporates data from 15 independent measurements.
[e]Rna14 molecular weight and equilibrium constant data were derived from global fitting of sedimentation equilibrium absorbance data measured at λ = 280 nm. The data were recorded at nine sample concentrations using rotor speeds of 8000, 10 000 and 12 000. The final global fit incorporates data from 12 independent measurements.
[f]All sedimentation equilibrium experiments were carried out in 20 mM Tris–HCl, pH 7.8, 150 mM NaCl, 0.5 mM TCEP at 20°C except Rna14 where the NaCl concentration was 200 mM.
[g]Rna14–Rna15 molecular weight and equilibrium constant data were derived from global fitting of sedimentation equilibrium absorbance data measured at λ = 280 and 250 nm. The data were recorded at nine sample concentrations using rotor speeds of 6000, 8000, 10 000 and 12 000. Data were fitted individually to determine the degree of concentration dependence and then separate global fits applied to data from each wavelength in order to derive equilibrium constants. The final value for K_a incorporates data from 27 independent measurements.

Table 2. Summary of sedimentation velocity data

Single component		Monomer–dimer equilibrium			Continuous	
		Monomer		Dimer		
$S_{20,w}$	8.1 ± 0.1	$S_{20,w}$	7.4 ± 0.15	8.4 ± 0.1	S_{app} C(S)	7.8 ± 0.05
$D_{20,w}$	3.7 ± 0.1	$D_{20,w}$	4.7 ± 0.1	2.7 ± 0.1	$S_{20,w}$	8.1 ± 0.05
M_w (S/D)	196 800	M_r	114 058	228 116	M_w C(M)	194 700
f/f_o	1.51	f/f_o	1.15	1.61		
		K_a (M^{-1})	$9 \times 10^5 \pm 10\%$			

Rna15NtD. However, when an equimolar mixture of Rna14 and Rna15 is applied across the biosensor surface a large response is observed, indicating that in combination the two proteins are able to bind to the RNA. To investigate this phenomenon further, a similar experiment was carried out using the bacterially expressed complex (Figure 5B). Again, a large response is observed indicating an interaction between the complex and the immobilized RNA. The response is titratable and global fitting of the sensograms from injection of 5 to 80 nM complex gives an equilibrium association constant of $\sim 2 \times 10^7$ M^{-1}.

RNA binding was also examined using gel retardation assays with the same *GAL7*-UTR ribo-oligonucleotide. Titration experiments for Rna15, Rna15NtD and the Rna14–Rna15 complex are shown in Figure 6. These experiments are carried out at a relatively high concentration; 1 μM *GAL7*-UTR titrated against 0.5–5 μM of each protein. Under these conditions, there is a tight association of the RNA with the Rna14–Rna15 complex. At the same time, there is no indication of RNA association with Rna15 alone or the Rna15 RRM, suggesting that in terms of K_d any interaction with the individual components must be much weaker than the micromolar concentrations used in these experiments. Similar gel retardation assays were performed using a control C-rich oligonucleotide (data not shown). The Rna14–Rna15 complex binds to this RNA with a similar affinity as it does to the *GAL7*-UTR RNA, whereas no interaction with individual proteins is observed. These results suggest that whilst Rna14–Rna15 assembly greatly enhances RNA-binding activity other proteins are likely to be required in order to attain sequence specificity.

The results of these RNA-binding experiments were somewhat unexpected, so RNA binding was also examined using UV cross-linking (Figure 7). The *GAL7*-UTR RNA was combined with increasing concentrations of either Rna14–Rna15 complex or Rna15 alone and irradiated with a handheld 254 nm UV lamp. In both cases, a cross-linked species (Ad1) corresponding to a Rna15-ribo-oligonucleotide adduct is formed (compare Figure 7A and B). The integrated band intensity corresponding to the amount of Ad1 produced is plotted as a function of protein concentration in Figure 7C and clearly indicates that the efficiency of this adduct formation is much higher when Rna15 is in a stoichiometric complex with Rna14. This suggests either that the Rna15 affinity for the RNA is much greater when bound to Rna14 or that the geometry of the Rna15–RNA interaction is different when in complex with Rna14. There is also a small amount of product formed, which may correspond to an Rna14-ribo-oligonucleotide adduct, Ad2, suggesting that Rna14 may be in direct contact with the RNA. This however remains to be tested.

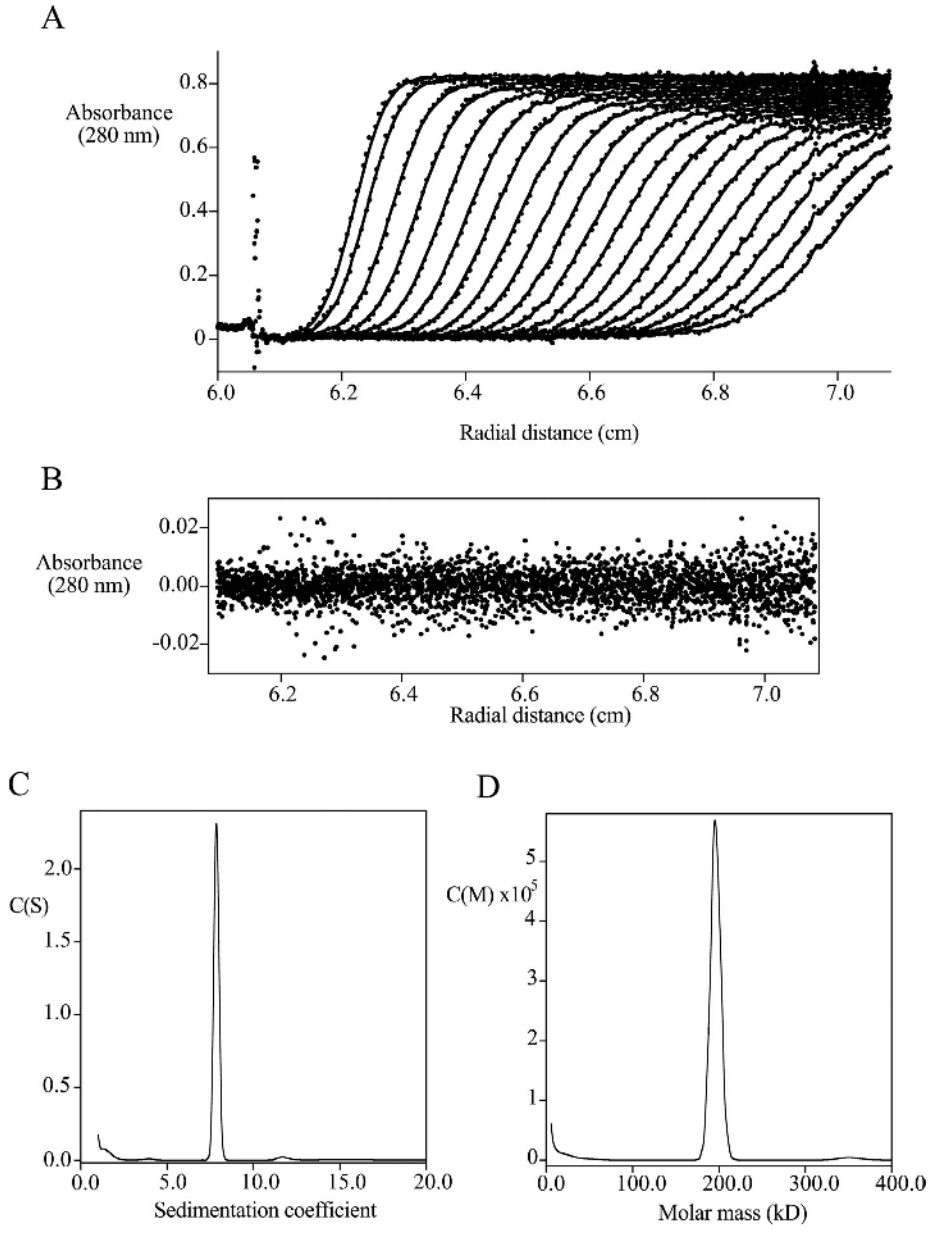

Figure 4. Analysis of the Rna14–Rna15 complex by sedimentation velocity. (**A**) Data produced from a single sedimentation velocity experiment at 35 000 r.p.m., scanned every 600 s. Lines are the best fit to the data using size distribution function C(S) and f/f_o = 1.51. (**B**) Residuals from the fit above. (**C**) C(S) function corresponding to the best fit in (A). (**D**) C(M) function corresponding to the best fit to the data in (A). The fit quality and residuals are comparable to the C(S) function.

DISCUSSION

Structure of the CFI complex and subunit assembly

Whilst the transmission electron micrographs and hydrodynamic analyses probe structure at low resolution, they have provided the first glimpses of the Rna14–Rna15 core of CFIA and given us new insight into a 3′ end processing machine. The two proteins appear to heterodimerize to form a distinct rod-shaped structure with an asymmetrically positioned 110° bend, giving rise to a long arm and a short arm (Figure 1D). Treating each arm as a cylinder, a molecular volume for an individual particle can be estimated to be ~125 000 Å^3. This is similar to the volume of 138 000 Å^3 calculated for a single 114 kDa protein with a partial specific volume of 0.729. The similarity between these values gives confidence to the idea that these bent rod structures are indeed Rna14–Rna15 heterodimers. However, in combination with Pcf11 and Clp1, in the context of CFIA, Rna14–Rna15 may be able to adopt a different conformation.

The heterodimers have the propensity to associate further into tetramers through an interface located near to the tip of their short arm. The finding that Rna14–Rna15 heterodimers

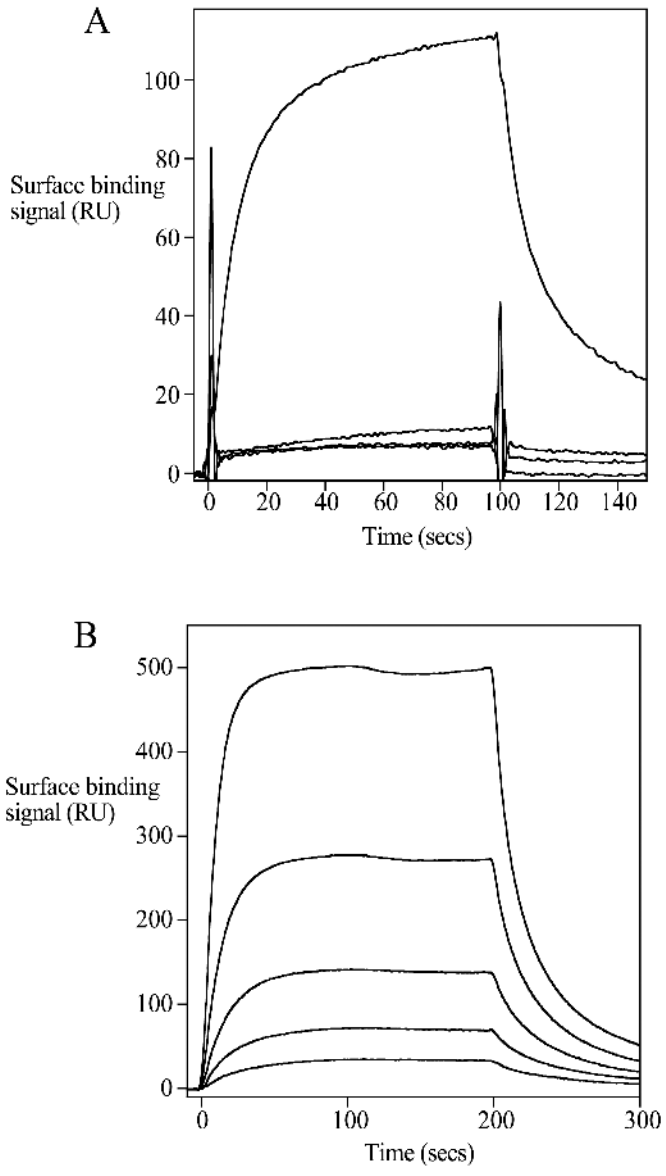

Figure 5. Analysis of RNA binding using SPR. (**A**) Sensograms from bottom to top are those produced from introduction of 80 nM Rna15, 80 nM Rna15NtD, 40 nM Rna14 and a mixture of 40 nM Rna14 + Rna15 over the surface of a biosensor chip coated with an immobilized *GAL7*-UTR ribo-oligoncleotide. (**B**) Sensograms produced from increasing concentrations of Rna14–Rna15 complex with immobilized *GAL7*-UTR ribo-oligoncleotide. The concentration of Rna14–Rna15 from bottom to top is 5, 10, 20, 40 and 80 nM.

associate weakly, $K_a = 6 \times 10^5$, into a tetrameric form is somewhat surprising. However, this complex represents a sub-assembly of CFIA and the whole complex contains two further components, Pcf11 and Clp1. It remains to be seen whether the Rna14–Rna15 complex assembles into tetramers within the native CFIA. The relatively weak association between heterodimers may well be stronger in combination with further Pcf11 or Clp1 interactions. Alternatively, Clp1 and or Pcf11 may interact preferentially with the heterodimeric form. It is also possible that the associative behaviour of Rna14–Rna15 complexes could be important in RNA binding. Around 44% of RRM-containing proteins have multiple copies of the domain (smart database http://smart.emblheidelberg.de/) and it has been proposed that multiple copies may be required in order to increase sequence specificity or to achieve a stronger RNA–protein interaction (32). Indeed Hrp1 contains two RRM domains and binds to RNA oligonucleotides in isolation [(33) and data not shown]. Since Rna15 contains only a single RRM, the tetramerization could provide the means to bring together two RRMs within the fully assembled CFIA complex.

RNA-binding

The examination of the RNA-binding properties of Rna15 and Rna14 by SPR analysis and gel retardation assays suggests that formation of an Rna14–Rna15 complex is required for a strong protein–RNA interaction to occur. This conclusion is supported by the fact that, under the conditions of both assays, neither protein showed detectable RNA binding in isolation. This is in contrast with previous reports that examined the RNA-binding properties of Rna15 using either UV cross-linking (23) or affinity capture methods (25). To investigate this apparent discrepancy further, we have also carried out UV cross-linking experiments and quantified the data in terms of the cross-linking efficiency. These results reveal that whilst Rna15 can be cross-linked to *GAL7* 3′-UTR-derived RNA, the efficiency of this process is greatly enhanced when Rna15 is associated with Rna14. Therefore, these data are consistent with the observations from the SPR and gel retardation studies. In general, UV cross-linking and affinity capture methods are particularly suitable for the detection of RNA–protein interactions. However, the inherent sensitivity of detection employed in both methods, often combined with a high protein to RNA ratio, make it possible to detect very small amounts of complex. Moreover, the likelihood is that under the high effective nucleotide concentration present on an affinity matrix (~1.6 mM nucleotide; poly(U) Sepharose 4B, Amersham Biosciences) some interaction with Rna15 alone will occur. In contrast, the gel retardation assays presented here demonstrate full-binding site occupancy with only a small excess of protein to RNA. Taken together, our data demonstrate both a large degree of complex formation, along with very great enhancement in RNA-binding activity, when both proteins are present. The question arises of whether the heterodimer, heterotetramer or both bind to RNA. Only one shifted species is observed in the gel retardation assays and it is unclear whether it corresponds to the dimeric or tetrameric form. Electron micrographs of the Rna14–Rna14 complex recorded in the presence of the *GAL7*-UTR ribo-oligonucleotide did not show any change in the shape of the complex or the ratio of dimers to tetramers (data not shown). These results indicate that RNA does not induce dimer association or tetramer dissociation and are consistent with both being able to bind RNA. This idea is supported by the fact that Rna14–Rna15 binds to RNA both at the nanomolar concentrations used in the SPR when the complex is almost entirely dimeric and at the micromolar concentrations of the gel retardation assays.

One rational for the large enhancement in binding is that the Rna14–Rna15 interaction results in the formation of an extended RNA-binding interface, where the RRM from Rna15 acts in combination with parts of Rna14, to produce

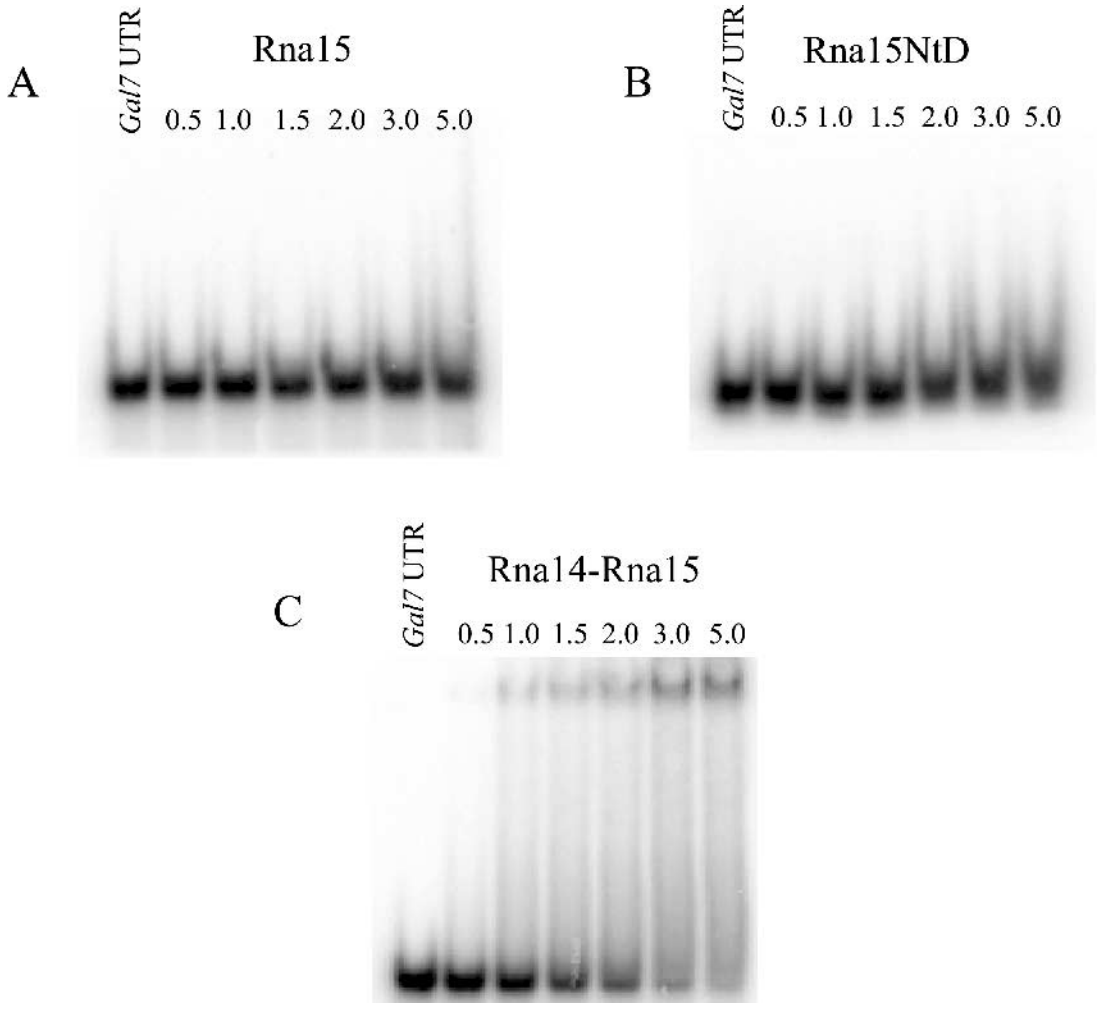

Figure 6. Gel retardation titration assays of Rna15 (**A**), Rna15NtD (**B**) and Rna14–Rna15 complex (**C**). Titrations were carried out with a fixed concentration of *GAL7*-UTR ribo-oligonucleotide (1.0 μM) and with the varying protein concentrations indicated above each track (μM).

the full-binding site. Another possibility is that Rna14–Rna15 complex formation may cause a structural transition in Rna15, Rna14 or even both proteins. This conformational change may be required in order to 'activate' the RNA-binding interface of the complex. This idea is consistent with the structure of the RRM from CstF-64, the human homologue of Rna15 (34). In this case, the RNA interface is in fact covered by a C-terminal helix in the free protein. The authors present evidence for an RNA-directed conformational change resulting in the destabilization of this C-terminal helix, allowing the interface to become accessible. A second precedent is provided by the RRM domain of Y14, a widely conserved core component of the exon-junction complex. Y14 forms a complex with another protein, Mago, and the two proteins are stably associated with mRNA during cytoplasmic export (35,36). In the recently determined crystal structures of the Mago–Y14 complexes (37–39) the β-sheet surface of the RRM domain of Y14, usually the RNA-binding interface of an RRM, is involved in an extensive interaction with Mago. The authors suggest that the RNA-binding surface of the RRM is released from the Mago interaction by a conformational change driven by the splicing reaction itself. This hypothesis is supported by the fact that splicing is required for Y14–Mago to interact with RNA. It is interesting to suppose that in CFIA the association of Rna14 with Rna15 may induce a similar effect in order to uncover the RRM at the N-terminus of Rna15. This in turn, may be part of an organized and directed assembly process and perhaps an important regulatory event controlling the RNA-binding activity of Rna15 both spatially and temporally.

Rna15 has been shown to be associated with the transcriptional co-activator Sub1 (27) and also the transcriptional activator Mbp1 (26). A model can be proposed whereby in early transcriptional events Rna15 is associated with factors, such as Sub1 and Mbp1, and in this situation Sub1 represses the termination activity of Rna15 (27). Interestingly, Sub1 appears to be involved in numerous, but mutually exclusive protein–protein interactions depending on the stage in the transcriptional cycle (40–42). It may be that upon recognition of transcription termination signals, Rna15 is released from Sub1 by competition with Rna14. Concomitantly, the CFIA RNA-binding interface would be activated or assembled, leading to the timely deployment of CFIA activity and

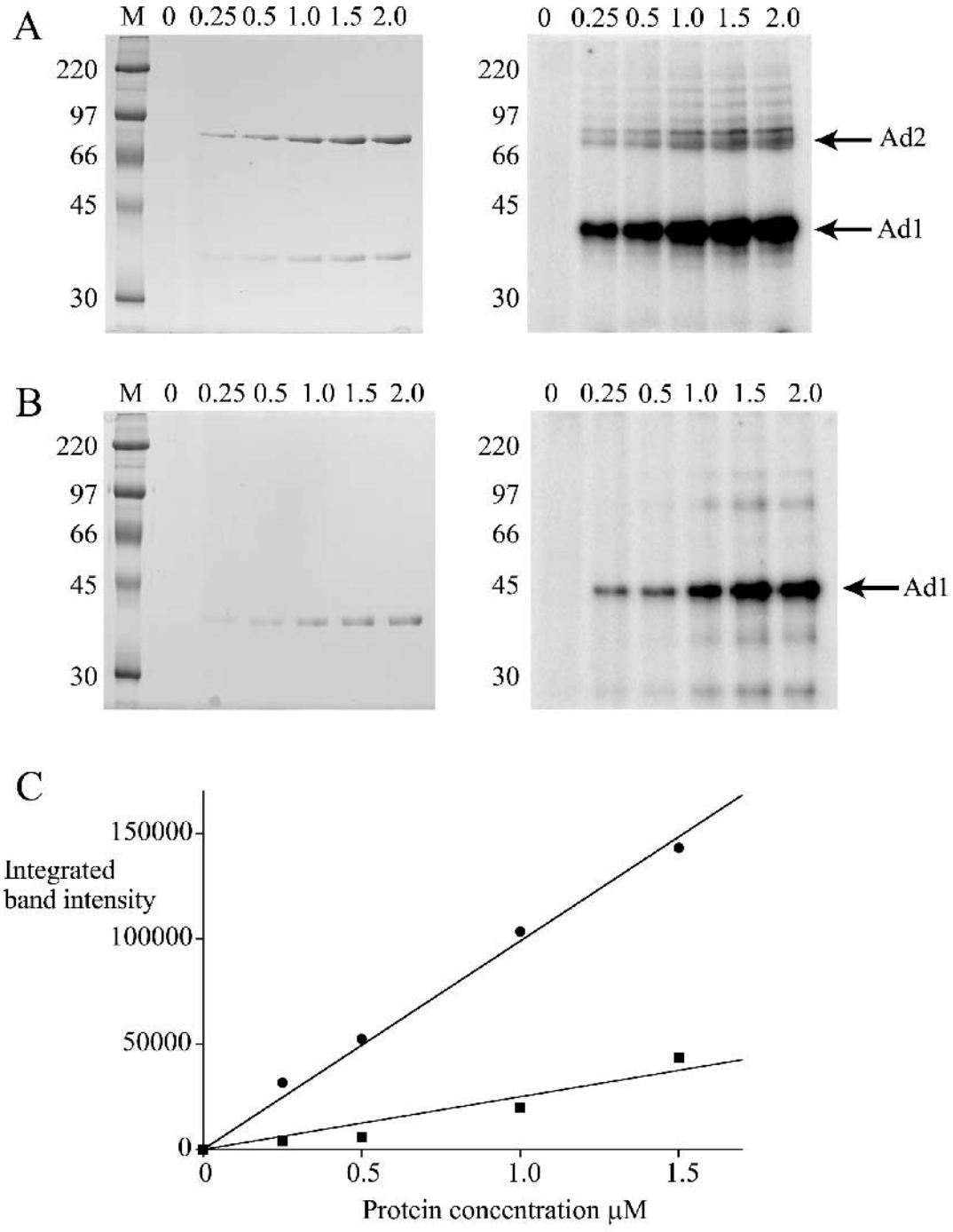

Figure 7. RNA binding using UV cross-linking. Samples were irradiated and the products were resolved by SDS–PAGE. (**A**) Coomassie blue staining (left) and autoradiography of UV cross-linking reactions for Rna14–Rna15 complex. (**B**) Coomassie blue staining and autoradiography of UV cross-linking reactions for Rna15; RNA–Rna15 adduct, Ad1; RNA–Rna14 adduct, Ad2. (**C**) Quantification of the amount of Ad1 produced in each cross-linking reaction; Rna14–Rna15 complex, closed circles; Rna15, closed squares. The integrated band intensity determined by phosphorimaging is plotted against protein concentration.

allowing subsequent termination, cleavage and polyadenylation to occur.

ACKNOWLEDGEMENTS

We thank Dr S. Smerdon and Dr S. Gamblin for critical reading of the manuscript, the Babraham Institute, Cambridge, for N-terminal sequencing and the NIMR graphics department for assistance with figure preparation.

REFERENCES

1. Zavolan,M., Kondo,S., Schonbach,C., Adachi,J., Hume,D.A., Hayashizaki,Y. and Gaasterland,T. (2003) Impact of alternative

initiation, splicing, and termination on the diversity of the mRNA transcripts encoded by the mouse transcriptome. *Genome Res.*, **13**, 1290–1300.
2. Beaudoing,E., Freier,S., Wyatt,J.R., Claverie,J.M. and Gautheret,D. (2000) Patterns of variant polyadenylation signal usage in human genes. *Genome Res.*, **10**, 1001–1010.
3. Pauws,E., van Kampen,A.H., van de Graaf,S.A., de Vijlder,J.J. and Ris-Stalpers,C. (2001) Heterogeneity in polyadenylation cleavage sites in mammalian mRNA sequences: implications for SAGE analysis. *Nucleic Acids Res.*, **29**, 1690–1694.
4. Iseli,C., Stevenson,B.J., de Souza,S.J., Samaia,H.B., Camargo,A.A., Buetow,K.H., Strausberg,R.L., Simpson,A.J., Bucher,P. and Jongeneel,C.V. (2002) Long-range heterogeneity at the 3′ ends of human mRNAs. *Genome Res.*, **12**, 1068–1074.
5. Chuvpilo,S., Zimmer,M., Kerstan,A., Glockner,J., Avots,A., Escher,C., Fischer,C., Inashkina,I., Jankevics,E., Berberich-Siebelt,F., Schmitt,E. and Serfling,E. (1999) Alternative polyadenylation events contribute to the induction of NF-ATc in effector T cells. *Immunity*, **10**, 261–269.
6. Kuersten,S. and Goodwin,E.B. (2003) The power of the 3′ UTR: translational control and development. *Nature Rev. Genet.*, **4**, 626–637.
7. Chen,J. and Moore,C. (1992) Separation of factors required for cleavage and polyadenylation of yeast pre-mRNA. *Mol. Cell. Biol.*, **12**, 3470–3481.
8. Kessler,M.M., Zhao,J. and Moore,C.L. (1996) Purification of the *Saccharomyces cerevisiae* cleavage/polyadenylation factor I. Separation into two components that are required for both cleavage and polyadenylation of mRNA 3′ ends. *J. Biol. Chem.*, **271**, 27167–27175.
9. Preker,P.J., Ohnacker,M., Minvielle-Sebastia,L. and Keller,W. (1997) A multisubunit 3′ end processing factor from yeast containing poly(A) polymerase and homologues of the subunits of mammalian cleavage and polyadenylation specificity factor. *EMBO J.*, **16**, 4727–4737.
10. Zhao,J., Kessler,M.M. and Moore,C.L. (1997) Cleavage factor II of *Saccharomyces cerevisiae* contains homologues to subunits of the mammalian cleavage/polyadenylation specificity factor and exhibits sequence-specific, ATP-dependent interaction with precursor RNA. *J. Biol. Chem.*, **272**, 10831–10838.
11. de Vries,H., Ruegsegger,U., Hubner,W., Friedlein,A., Langen,H. and Keller,W. (2000) Human pre-mRNA cleavage factor II(m) contains homologs of yeast proteins and bridges two other cleavage factors. *EMBO J.*, **19**, 5895–5904.
12. Barilla,D., Lee,B.A. and Proudfoot,N.J. (2001) Cleavage/polyadenylation factor IA associates with the carboxyl-terminal domain of RNA polymerase II in *Saccharomyces cerevisiae*. *Proc. Natl Acad. Sci. USA*, **98**, 445–450.
13. Licatalosi,D.D., Geiger,G., Minet,M., Schroeder,S., Cilli,K., McNeil,J.B. and Bentley,D.L. (2002) Functional interaction of yeast pre-mRNA 3′ end processing factors with RNA polymerase II. *Mol. Cell*, **9**, 1101–1111.
14. Sadowski,M., Dichtl,B., Hubner,W. and Keller,W. (2003) Independent functions of yeast Pcf11p in pre-mRNA 3′ end processing and in transcription termination. *EMBO J.*, **22**, 2167–2177.
15. Amrani,N., Minet,M., Le Gouar,M., Lacroute,F. and Wyers,F. (1997) Yeast Pab1 interacts with Rna15 and participates in the control of the poly(A) tail length *in vitro*. *Mol. Cell. Biol.*, **17**, 3694–3701.
16. Amrani,N., Minet,M., Wyers,F., Dufour,M.E., Aggerbeck,L.P. and Lacroute,F. (1997) PCF11 encodes a third protein component of yeast cleavage and polyadenylation factor I. *Mol. Cell. Biol.*, **17**, 1102–1109.
17. Kessler,M.M., Henry,M.F., Shen,E., Zhao,J., Gross,S., Silver,P.A. and Moore,C.L. (1997) Hrp1, a sequence-specific RNA-binding protein that shuttles between the nucleus and the cytoplasm, is required for mRNA 3′-end formation in yeast. *Genes Dev.*, **11**, 2545–2556.
18. Gross,S. and Moore,C. (2001) Five subunits are required for reconstitution of the cleavage and polyadenylation activities of *Saccharomyces cerevisiae* cleavage factor I. *Proc. Natl Acad. Sci. USA*, **98**, 6080–6085.
19. Nedea,E., He,X., Kim,M., Pootoolal,J., Zhong,G., Canadien,V., Hughes,T., Buratowski,S., Moore,C.L. and Greenblatt,J. (2003) Organization and function of APT, a subcomplex of the yeast cleavage and polyadenylation factor involved in the formation of mRNA and small nucleolar RNA 3′-ends. *J. Biol. Chem.*, **278**, 33000–33010.
20. Gavin,A.C., Bosche,M., Krause,R., Grandi,P., Marzioch,M., Bauer,A., Schultz,J., Rick,J.M., Michon,A.M., Cruciat,C.M., *et al.* (2002) Functional organization of the yeast proteome by systematic analysis of protein complexes. *Nature*, **415**, 141–147.
21. Preker,P.J. and Keller,W. (1998) The HAT helix, a repetitive motif implicated in RNA processing. *Trends Biochem. Sci.*, **23**, 15–16.
22. Minvielle-Sebastia,L., Preker,P.J. and Keller,W. (1994) RNA14 and RNA15 proteins as components of a yeast pre-mRNA 3′-end processing factor. *Science*, **266**, 1702–1705.
23. Gross,S. and Moore,C.L. (2001) Rna15 interaction with the A-rich yeast polyadenylation signal is an essential step in mRNA 3′-end formation. *Mol. Cell. Biol.*, **21**, 8045–8055.
24. Minvielle-Sebastia,L., Beyer,K., Krecic,A.M., Hector,R.E., Swanson,M.S. and Keller,W. (1998) Control of cleavage site selection during mRNA 3′ end formation by a yeast hnRNP. *EMBO J.*, **17**, 7454–7468.
25. Birse,C.E., Minvielle-Sebastia,L., Lee,B.A., Keller,W. and Proudfoot,N.J. (1998) Coupling termination of transcription to messenger RNA maturation in yeast. *Science*, **280**, 298–301.
26. Aranda,A. and Proudfoot,N. (2001) Transcriptional termination factors for RNA polymerase II in yeast. *Mol. Cell*, **7**, 1003–1011.
27. Calvo,O. and Manley,J.L. (2001) Evolutionarily conserved interaction between CstF-64 and PC4 links transcription, polyadenylation, and termination. *Mol. Cell*, **7**, 1013–1023.
28. Laue,T.M., Shah,B.D., Ridgeway,T.M. and Pelletier,S.L. (1992) Computer-aided interpretation of analytical sedimentation data for proteins. In Harding,S.E., Rowe,A.J. and Horton,J.C. (eds), *Analytical Ultracentrifugation in Biochemistry and Polymer Science*. The Royal Society of Chemistry: Cambridge, UK. pp. 90–125.
29. Schuck,P., Perugini,M.A., Gonzales,N.R., Howlett,G.J. and Schubert,D. (2002) Size-distribution analysis of proteins by analytical ultracentrifugation: strategies and application to model systems. *Biophys. J.*, **82**, 1096–1111.
30. Schuck,P. (2000) Size-distribution analysis of macromolecules by sedimentation velocity ultracentrifugation and lamm equation modeling. *Biophys. J.*, **78**, 1606–1619.
31. Taylor,I.A., Davis,K.G., Watts,D. and Kneale,G.G. (1994) DNA-binding induces a major structural transition in a type I methyltransferase. *EMBO J.*, **13**, 5772–5778.
32. Xu,R.M., Jokhan,L., Cheng,X., Mayeda,A. and Krainer,A.R. (1997) Crystal structure of human UP1, the domain of hnRNP A1 that contains two RNA-recognition motifs. *Structure*, **5**, 559–570.
33. Valentini,S.R., Weiss,V.H. and Silver,P.A. (1999) Arginine methylation and binding of Hrp1p to the efficiency element for mRNA 3′-end formation. *RNA*, **5**, 272–280.
34. Perez Canadillas,J.M. and Varani,G. (2003) Recognition of GU-rich polyadenylation regulatory elements by human CstF-64 protein. *EMBO J.*, **22**, 2821–2830.
35. Dostie,J. and Dreyfuss,G. (2002) Translation is required to remove Y14 from mRNAs in the cytoplasm. *Curr. Biol.*, **12**, 1060–1067.
36. Kataoka,N., Diem,M.D., Kim,V.N., Yong,J. and Dreyfuss,G. (2001) Magoh, a human homolog of *Drosophila* mago nashi protein, is a component of the splicing-dependent exon–exon junction complex. *EMBO J.*, **20**, 6424–6433.
37. Fribourg,S., Gatfield,D., Izaurralde,E. and Conti,E. (2003) A novel mode of RBD–protein recognition in the Y14–Mago complex. *Nat. Struct. Biol.*, **10**, 433–439.
38. Lau,C.K., Diem,M.D., Dreyfuss,G. and Van Duyne,G.D. (2003) Structure of the y14-magoh core of the exon junction complex. *Curr. Biol.*, **13**, 933–941.
39. Shi,H. and Xu,R.M. (2003) Crystal structure of the *Drosophila* Mago nashi-Y14 complex. *Genes Dev.*, **17**, 971–976.
40. Wu,W.H., Pinto,I., Chen,B.S. and Hampsey,M. (1999) Mutational analysis of yeast TFIIB. A functional relationship between Ssu72 and Sub1/Tsp1 defined by allele-specific interactions with TFIIB. *Genetics*, **153**, 643–652.
41. He,X., Khan,A.U., Cheng,H., Pappas,D.L.,Jr, Hampsey,M. and Moore,C.L. (2003) Functional interactions between the transcription and mRNA 3′ end processing machineries mediated by Ssu72 and Sub1. *Genes Dev.*, **17**, 1030–1042.
42. Knaus,R., Pollock,R. and Guarente,L. (1996) Yeast SUB1 is a suppressor of TFIIB mutations and has homology to the human co-activator PC4. *EMBO J.*, **15**, 1933–1940.